Sustainable Multifunctionality: Bio-inspired Printing of Nanocellulose Aerogel Acoustical Materials *Guang Yang, Amulya Lomte, Bhisham Sharma*, Shuting Lei, Dong Lin**

Guang Yang, Shuting Lei
Department of Industrial and Manufacturing Systems Engineering
Kansas State University
Manhattan, KS, 66506, USA

Amulya Lomte
Department of Aerospace Engineering
Wichita State University
Wichita, KS, 67260, USA

Bhisham Sharma
Mechanical Engineering-Engineering Mechanics
Michigan Technological University
1400 Townsend Drive, Houghton, MI, 49931, USA
E-mail: bnsharma@mtu.edu

Dong Lin
School of Mechanical, Industrial, and Manufacturing Engineering
Oregon State University
218 Dearborn Hall, Corvallis, OR, 97331, USA
E-mail: dong.lin@oregonstate.edu

Keywords: 3D freeze printing, nanocellulose, noise control, bidirectional pore orientation, multifunctional materials

Abstract

We demonstrate the three-dimensional freeze printing (3DFP) of nanocellulose aerogels with large-scale aligned pore orientations as a sustainable alternative to current acoustical materials. In contrast with the unidirectional pore network orientations obtained from current 3DFP techniques, we achieve a bidirectional orientation by using an inhomogeneous printing substrate to alter the

thermal gradient within the print volume. The microstructural morphology shows that bidirectional printing results in a two-dimensional pore orientation, with comparatively thinner pore walls and larger pore widths. Acoustic measurements reveal that altering the pore network characteristics significantly affects the acoustical behavior of the printed CNC aerogels; the wider pores allow the bidirectional CNC aerogels to provide higher sound absorption performance at lower frequencies than the unidirectional samples. Notably, both 3D Freeze printed CNC aerogels provide substantially higher sound transmission loss performance as compared to current acoustical materials. The unidirectional pore structure results in CNC aerogels with higher stiffness and improved energy absorption performance, with both 3D freeze printed CNC aerogels outperforming other CNC aerogel materials in their stiffness-to-density ratios. The ability to simultaneously control their pore orientation and macrostructural geometry paves the way for printing complex shaped CNC aerogel structures for multifunctional noise control applications.

1. Introduction

Noise pollution is a pressing societal concern, both for human health and the environment. Health effects stemming from daily noise exposure include hearing loss and tinnitus, [1] sleep disturbance, [2] heightened stress, [3] mental health disorders, [4] cardiovascular diseases, [5] and impaired cognitive development in children. [6] According to a World Health Organization summary report, [7] daily noise exposure results in an annual loss of at least one million healthy life years. Excessive noise is also an ecological concern: [8] it jeopardizes habitats, interferes with wildlife communication, shifts predatory-prey dynamics, and alters long established migration routes. These concerns are reflected in the increasingly stringent noise regulations and certification requirements being issued by regulatory bodies throughout the world. [9]

Current noise abatement technologies can be classified into active and passive systems. Active noise reduction systems use electronic methods to cancel noise by generating sound waves with an inverted phase relative to the unwanted waves. [10] Such systems are highly effective for attenuating noise with narrow banded frequency profiles; however, their constant power supply requirement limits their use for applications requiring energy and cost efficiency. Therefore, passive noise control methods continue to be the predominant method for most applications. Passive techniques may be further subclassified into reactive and resistive systems. [11] Reactive systems, such as automotive silences, bass traps, and duct mufflers, rely on the energy losses occurring due to Helmholtz resonances or impedance discontinuities to attenuate sound waves. On the other hand, resistive systems are primarily comprised of porous materials that absorb incident sound waves by dissipating their acoustic energy via viscous and thermal losses. [12] This loss mechanism, coupled with their easier implementation and lower operational costs, makes them the preferred noise control solution for a majority of applications. However, state-of-the-art porous materials, [13] such as acoustic foams and glass fiber sheets, offer low mechanical stiffness and are highly compliant. This compliance limits their use for structural applications and makes it difficult to accurately characterize their acoustical properties - unintentional compression or aeration can skew the measured impedances and transport properties.[14] The traditional methods used to manufacture these materials cause additional uncertainties: they result in a stochastic pore architecture, which introduces batch-to-batch property variations and restricts the deliberate engineering of pore shapes to attain optimal performance for targeted uses. [15] Currently, acoustic foams are predominantly made from polyurethane or other synthetic polymers that are derived from fossil fuels. The flammability characteristics of such materials preclude their use for high temperature applications typically encountered in aerospace and other engineering domains. Their

manufacturing processes often involve chemicals and processes that are harmful to the environment. Importantly, these materials are not biodegradable and can be difficult to recycle-their durability allows them to persist in landfills for many years after their disposal.

Cellulose, found in plant cell walls and among the earth's most abundantly available biopolymers, is a potential sustainable alternative. [16] Historically used in the production of paper and textiles, the recent necessity for sustainability has spurred researchers to explore the use of cellulose-based materials for a broader range of applications. [16-17] However, their broader engineering use is hindered by their limited durability and uniformity. The advent of nanocellulose provides a way to overcome these barriers by introducing superior characteristics, such as improved mechanical stiffness, decreased thermal expansion, and lower density. [18] Notably, recent research shows that deriving aerogels using nanocellulose can provide unique combinations of ultralow density and exceptional mechanical properties. [19] Consequently, nanocellulose aerogels are a subject of growing research interest across diverse fields, including their use in energy storage devices, [20] thermal insulation materials, [21] and biomedical scaffolds. [22] Similar to other aerogels, nanocellulose aerogels are currently fabricated using either supercritical drying or freeze-drying to avoid surface tension issues damaging the solid pore network; [19] the specific process choice typically depends on the material and application requirements. While both processes result in aerogels with stochastic pore networks, their network can be more precisely controlled using the freeze-drying method by preceding the drying step with freeze-casting or ice-templating, [23] wherein the aerogel precursor's colloidal suspension is frozen under controlled thermal conditions into the desired macrostructural shape using a thermally insulated mold. As the suspension freezes, the precursor molecules infiltrate the gaps between the growing solvent crystals, creating a densely packed pore network whose structural characteristics are governed by

the surrounding thermal conditions. [24] The solvent ice crystals are then sublimated during the subsequent freeze-drying step to obtain the desired porous microstructure. This technique has been used to produce aerogels from ceramics, [23a, 25] metals, [26] polymers, [27] and carbon nanomaterials. [28]

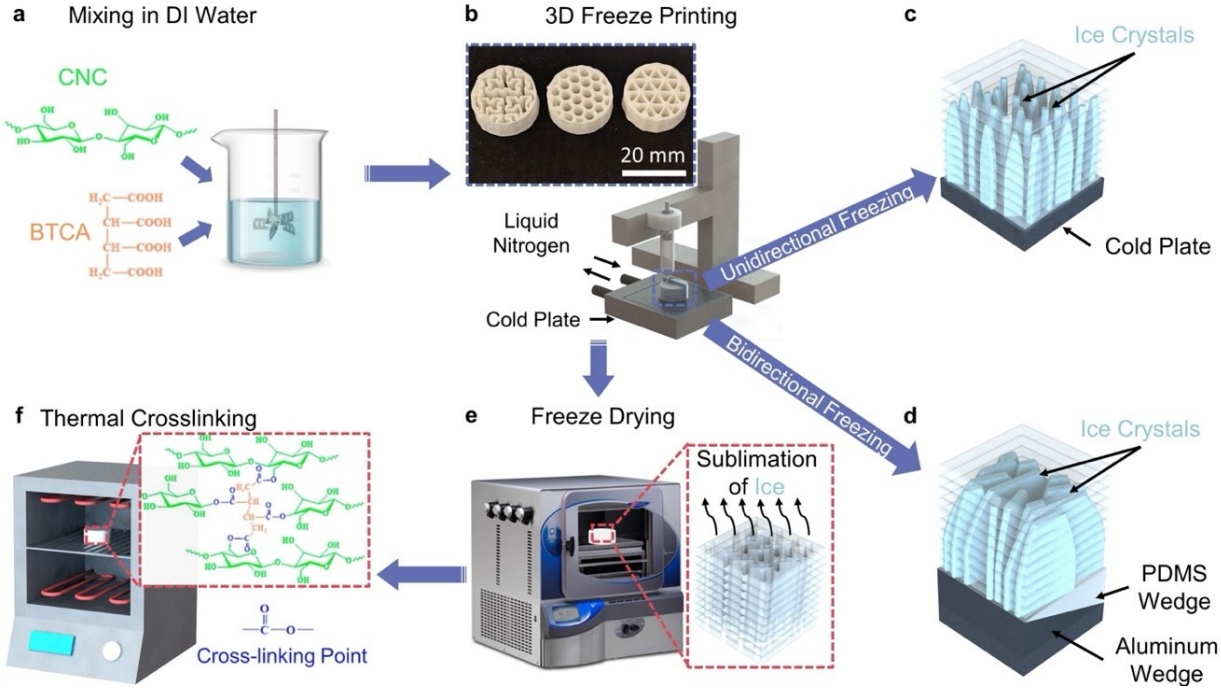

Figure 1. Schematic of the 3D Freeze Printing (3DFP) and post processing. a) Ink preparation. b) 3DFP setup. c) Unidirectional freezing setup. d) Bidirectional freezing setup. e) Freeze-drying process. f) Crosslinking process.

The requirement of a mold to obtain the desired macrostructural geometries constrains the feasibility of using freeze-casting to fabricate complex three-dimensional aerogel structures. Our recent efforts show that this mold constraint can be eliminated by combining freeze-casting with extrusion-based additive manufacturing, termed three-dimensional freeze printing (3DFP). [24, 29] As illustrated in **Figure 1**, in 3DFP, the aerogel ink is extruded from a printing nozzle and deposited layer-by-layer onto a chilled print bed with precisely controlled temperature (from -180°C to 120°C). As the ink is deposited on the cold print bed, the solvent crystallizes, allowing the

precursor molecules to create a densely packed pore network by infiltrating the gaps between the growing crystals. [24] During the subsequent freeze-drying step, the solvent crystals are sublimated, and the precursor molecules thermally crosslink to form the final aerogel with the desired macrostructure. Similar to other extrusion-based 3D printing processes, this method allows the fabrication of complex macrostructural geometries without the constraints associated with a traditional molding process, as shown in Figure 1b insert. For aerogel structures fabricated using 3DFP, the pore network characteristics are determined by the solvent ice crystal growth dynamics and the resultant inter-crystal gap geometry. [30] As depicted in Figure 1c, in traditional 3DFP, the use of a uniform flat plate results in a unidirectional thermal gradient orthogonal to the print bed, restricting the crystal align along the vertical direction and resulting in a corresponding unidirectional pore network. In this method, the pore widths can be controlled by controlling the temperature gradient of the uniform print bed. However, our unidirectional 3DFP is limited to aligning pores solely in the orthogonal direction. This limitation in controlling pore orientation hinders the capability of fabricating aerogel architectures with optimized microporous network properties s for application-specific characteristics.

Here, we overcome this limitation and demonstrate the fabrication of CNC aerogels with a two-dimensional, laminated pore orientation control for multifunctional noise reduction applications. We achieve this by replacing the uniform print bed with a print substrate that combines a polydimethylsiloxane (PDMS) and an aluminum wedge to provide a directional thermal gradient within the print volume, consequently controlling the pore orientation along two directions. As depicted in Figure 1e, we position the flat surface of the aluminum wedge directly on the cold plate and then attach a PDMS wedge to the top surface; both wedges are identical in size and are connected along a 20° wedge angle to ensure a horizontal print bed. The significant

disparity between the thermal conductivities of the aluminum wedge (239 $Wm^{-1}K^{-1}$) and the PDMS wedge (0.15 $Wm^{-1}K^{-1}$) generates an additional thermal gradient along the horizontal direction. This bidirectional thermal gradient alters the previously vertical orientation of the ice crystals and consequently results in CNC aerogels with a bidirectional pore network. [30] Our results show that such bidirectional CNC aerogels provide vastly superior sound absorption and transmission loss properties as compared to current acoustical materials used for noise reduction applications. Further, we show that CNC aerogels fabricated using unidirectional and bidirectional 3DFP provide better mechanical and functional properties than those fabricated using other methods. Thus, the presented method provides a novel route toward engineering sustainable and multifunctional noise reduction solutions for advanced applications.

2. Results and Discussion

The differences between the overall pore structure of samples fabricated using unidirectional and bidirectional 3DFP can be seen in the scanning electron microscopy (SEM) images shown in Figure 2. In addition to the differences in the pore alignment, as seen from Figures 2b and 2f, altering the temperature gradient orientation also affects the wall thickness and pore widths. In the bidirectional 3DFP process, the ice crystals underwent reduced growth rates and extended fusion durations, leading to the enlargement and elongation of the ice crystals. Additionally, the CNC walls underwent increased compression, leading to thinner walls. Overall, as measured over a 12.5 mm sample area, bidirectional printing results in thinner walls with a tighter wall thickness distribution (Figure 2d) as compared to the unidirectionally printed sample. As expected, this reduction in wall thickness is associated with an enlargement in the open pore widths of the bidirectional sample (Figure 2h). The average pore width-reflecting the spacing between the

adjacent ice crystals-of the bidirectional samples is 62 μm while that of the unidirectional samples is 31 μm.

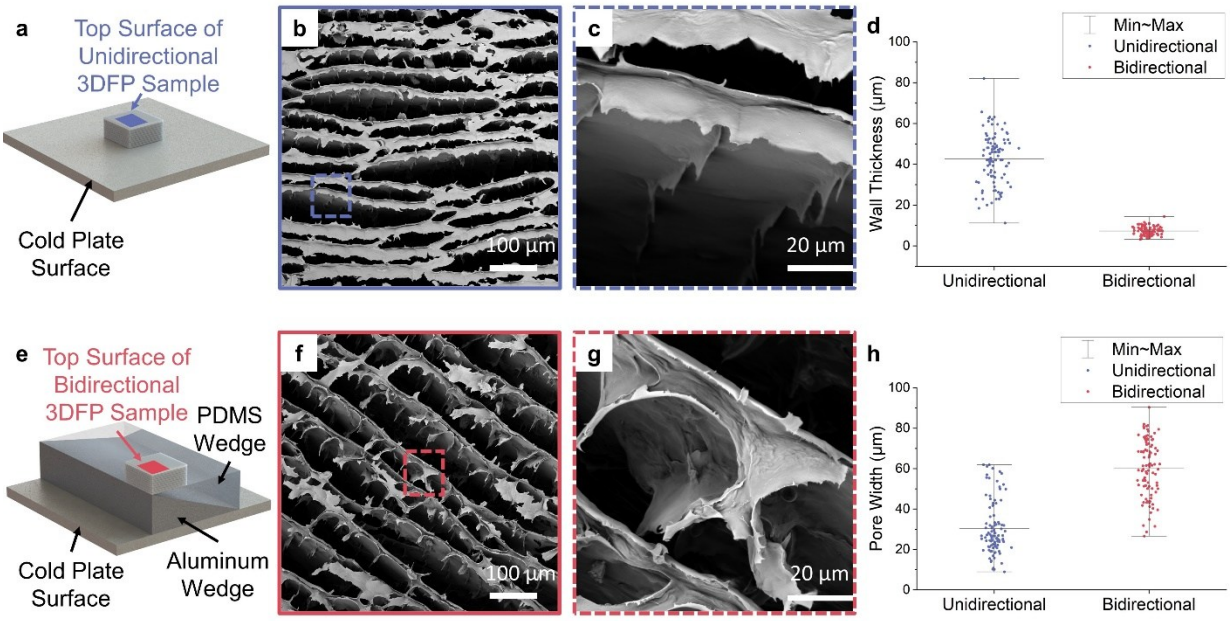

Figure 2. Scanning electron microscopy (SEM) images of 3D freeze printed samples. a) Schematics of unidirectional freeze casting setup. b)-c) Top views of aerogels under unidirectional freeze casting. d) Wall thickness of the aerogels. e) Schematics of bidirectional freeze casting setup. f)-g) Top views of aerogels under bidirectional freeze casting. h) Pore width of the aerogels.

The underlying pore network of open-celled porous materials controls their sound absorption performance. [12] As sound waves travel through a porous material the incident acoustic energy gets absorbed due to the frictional and thermal losses occurring at the fluid-solid interfaces within the pore channels. The amount of energy dissipated is thus intrinsically dependent on the geometrical parameters of the pore network-notably the pore width, orientation, and network tortuosity. [12] The sound absorption coefficients of rigidly backed unidirectional and bidirectional CNC aerogel

samples of 12.7 mm thickness under normal incidence conditions are compared in Figure 3c. The measurements are performed over a frequency range from 600 Hz to 6100 Hz using the 2-microphone normal incidence impedance tube technique, as prescribed by ASTM E1050-19. The results are obtained by averaging the sound absorption measurements performed for four different samples of each type. Measurements labeled side A are performed with the bottom surface-i.e., the surface in contact with the print plate-facing the incident waves while side B refers to the top surface of the sample. The two sides of the test samples are shown in Figure 3b.

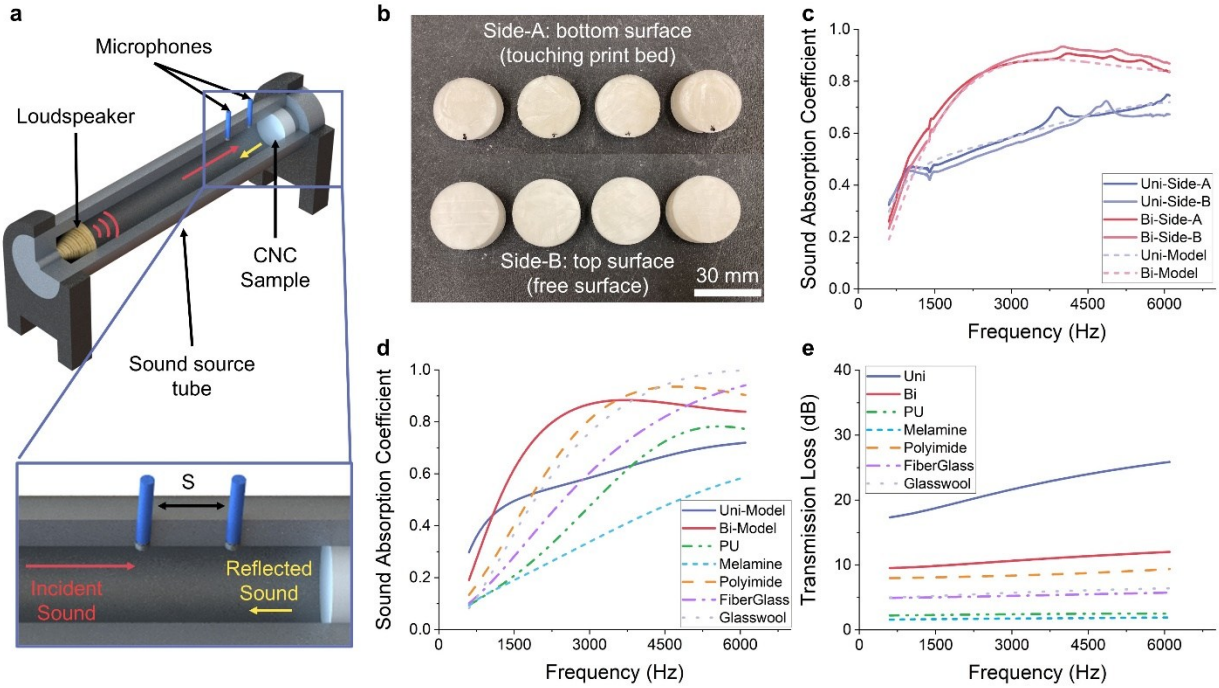

Figure 3. Acoustical characteristics of unidirectional and bidirectional CNC aerogels and their comparison with other acoustical materials. a) Test samples used characterization showing the two different sides of each sample. b) Comparison of the sound absorption measurement of the unidirectional and bidirectional samples. The measured data are represented using solid lines while the absorptions predicted by the inverse characterization approach are represented using dashed lines. c) Comparison of the sound absorption coefficients of the 3D freeze printed CNC aerogels

with other acoustical materials. d) Comparison of the sound transmission loss curves of the 3D freeze printed CNC aerogels with other acoustical materials.

The absorption measurements show that the differences in the pore structure of the unidirectional and bidirectional samples result in markedly different sound absorption performance over the measurement range. While both absorbers provide broadband performance reminiscent of other resistive porous materials [31], the bidirectional pore structure significantly improves the absorption coefficient, absorbing more than 60% of the incident acoustic energy for all frequencies above 1500 Hz. Further, minimal differences are observed between the two sides of each sample, indicating the through-thickness uniformity of the 3D printed samples. Note that the observed differences are within the uncertainty bounds of the test procedure and the sample-to-sample property variations observed for sound absorbers printed using other additive techniques. [14-15]

Table 1. Acoustical transport parameters estimated by the inverse characterization approach.

CNC Aerogel Type	**Porosity**	**Resistivity [Ns/m^4]**	**Tortuosity**	**Viscous Characteristic Length [μm]**	**Thermal Characteristic Length [μm]**
Unidirectional	99%	390,287	4.309	37.4	37.4
Bidirectional	99%	126,274	2.89	68.1	68.1

The differences in the pore structure and its effect on the overall acoustical performance are further quantified by extracting the relevant acoustic transport parameters using an inverse characterization approach. [32] Here, we model both absorbers as acoustically rigid using the Johnson-Champoux-Allard (JCA) formulation. [12, 32] The estimated acoustic transport properties are provided in Table 1. The accuracy of the model is verified by comparing the predicted and measured sound absorption curves in Figure 3c. Both predictions (dashed lines) match the measured data (solid lines), establishing the validity of the JCA formulation for modeling the acoustical behavior of 3D printed CNC aerogel materials. As expected from the SEM observations, the thicker cell walls and narrower average pore width of the unidirectional samples results in a comparatively higher static airflow resistivity and lower viscous and thermal characteristics lengths. The estimated viscous and thermal characteristic lengths-strongly correlated to the pore and throat diameters, [12, 32] respectively, and the dominant parameters controlling the visco-thermal effects at medium and high acoustical frequencies-compare well with the pore width distributions obtained from the SEM characterization (Figure 2h). Further, the inverse characterization predicts that the unidirectional thermal gradient results in a more tortuous pore network. A higher tortuosity typically improves the sound absorption performance by increasing the path length traversed by the sound waves. However, the lower sound absorption of the unidirectionally printed samples suggests that their smaller pore width results in an excessively high airflow resistance, resulting in reflecting the incident sound waves rather than absorbing them.

Figures 3d and 3e compare the predicted normal incidence sound absorption and transmission loss properties of the unidirectional and bidirectional CNC aerogel samples with the predicted properties of 12.7 mm thick samples of other widely used acoustical materials: [12, 32-33] polyurethane, melamine, polyimide, fiberglass, and glass wool. Figure 3d shows that both 3D

printed CNC aerogels provide better sound absorption performance than the current acoustical materials at frequencies below 2000 Hz, with the bidirectional CNC aerogel providing the highest absorption until approximately 3000 Hz. Further, Figure 3e shows that both CNC aerogels significantly outperform all the other materials in their sound transmission loss performance. Notably, the unidirectional pore network results in transmission loss that is more than 200% higher at lower frequencies and more than 300% higher at higher frequencies as compared to the polyimide sample of the same thickness. The differences between the transmission loss properties of the bidirectional and unidirectional samples are in line with the previous observations indicating that the narrowed pore widths of the unidirectional CNC aerogels result in higher reflection, reducing the acoustic energy absorbed by the material while increasing the transmission loss.

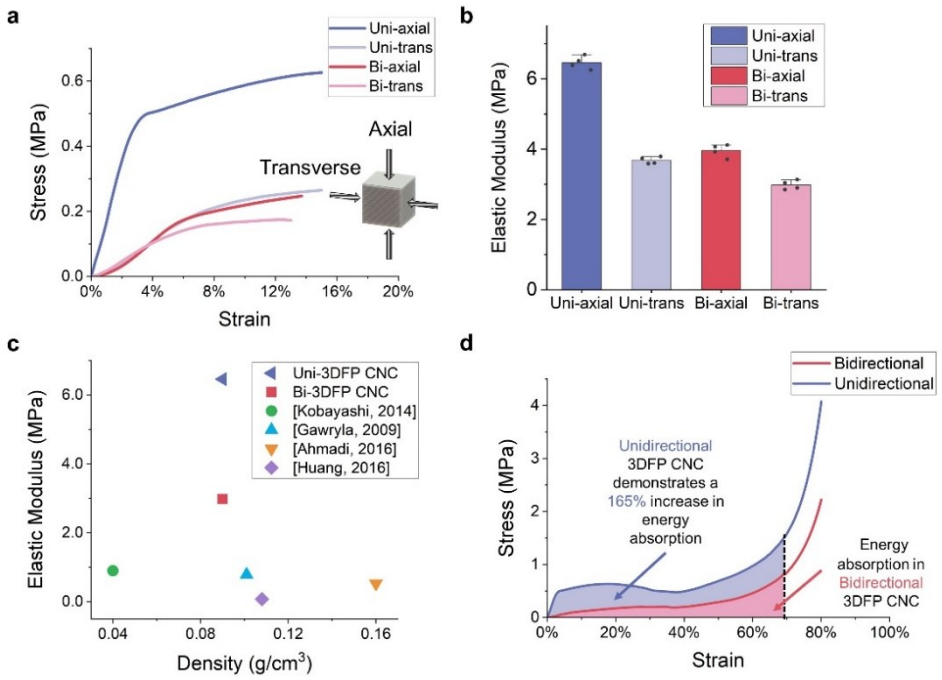

Figure 4. Mechanical properties of the CNC aerogel. a) Comparison of stress-strain behavior of unidirectional and bidirectional CNC aerogels under uniaxial and biaxial compressive loading. b) Comparison of their elastic moduli from the stress-strain curves. c) Property map of elastic

modulus versus density for CNC based aerogels. d) Comparison of the energy absorption behavior of unidirectional and bidirectional CNC aerogels at low strain rates.

The pore network differences between the unidirectional and bidirectional CNC aerogels also influences their mechanical stiffness properties. [34] Figure 4a compares their stress-strain curves when subjected to compression between two parallel plates using a universal testing machine. The testing was conducted by centering cubic samples on the lower stationary plate and compressing them at a constant rate of 1 $mm.min^{-1}$ using the upper parallel plate. Using the cubic samples allows application of the load along the parallel (axial) and perpendicular (transverse) directions with respect to the freezing direction. As expected, altering the temperature gradient with a bi-directional 3DFP setup during printing drastically changes the mechanical performance of the resulting CNC aerogels. The vertical cell wall orientation of unidirectional samples allows them to resist a significantly higher amount of stress as compared to the bidirectional samples when compressed axially, i.e., parallel to the cell wall direction. When loaded along the transverse direction, though the initial stress-strain behavior of both samples is similar, the bidirectional sample yields at a lower stress. Interestingly, both samples exhibit a sharper transition from the elastic to the plastic regime under axial loading as compared to the gradual transition observed under transverse loading. Calculating the elastic modulus using the linear regime of the stress-strain curves shows that unidirectional printing results in CNC aerogels that are stiffer along the axial as well as transverse directions. Notably, due to the uniaxial orientation of their pore walls along the loading direction, the unidirectional sample exhibits an axial elastic modulus approximately 45% higher than the bidirectional sample. Figure 4c compares the elastic moduli of the unidirectional and bidirectional 3D printed CNC aerogels with other previously reported CNC

aerogel-based materials as a function of their mass density. [23c, 35] It can be seen that the controlled pore structure of the unidirectional and bidirectional CNC aerogels results in significantly higher stiffness-to-density ratios, with both materials outperforming other CNC aerogels.

The energy absorption performance of the unidirectional and bidirectional aerogels at low strain-rates are compared in Figure 4d. Overall, both materials display stress-strain profiles typically observed for porous materials: [34] the materials initially deform linear elastically, followed by a stress plateau region with large strain increments, eventually densifying and displaying a sharp increase in the stress. The higher yield stress of the unidirectional aerogels results in a higher plateau stress and a flatter plateau stress profile. Comparatively, their bidirectional orientation and narrower pore wall thickness results in a more gradual pore channel collapse, resulting in a plateau stress profile where the stress is slowly increasing with increasing strain values until the neighboring pore walls come into contact and the sample begins densifying. The larger pore widths of the bidirectional CNC aerogels result in a higher densification strain as compared to the unidirectional CNC aerogels. Overall, the higher plateau stress of the unidirectional CNC aerogels provides approximately 165% higher energy absorption as compared to the bidirectional aerogels, where the energy absorption is calculated as the area under the individual curves until the densification strain.

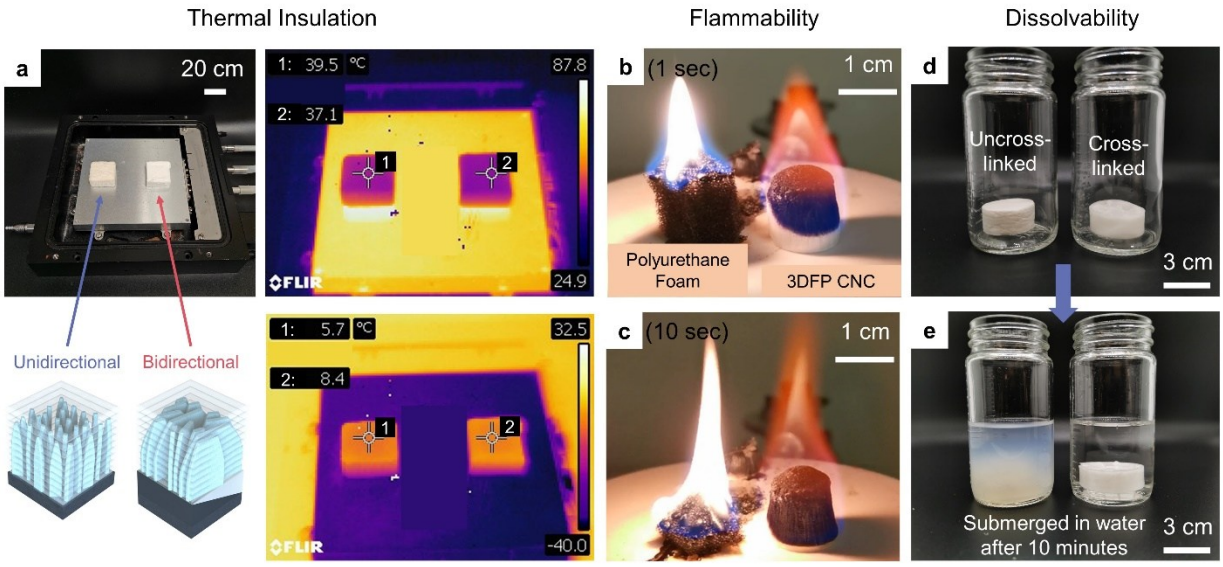

Figure 5. Multifunctional performance of 3D Freeze printed CNC aerogels. a) Comparison of thermal insulation abilities of unidirectional and bidirectional CNC aerogels. b-c) Flammability comparison of unidirectional CNC aerogel with polyurethane foam. d-e) Dissolvability comparison of crosslinked and un-crosslinked CNC aerogels.

Figure 5 demonstrates the other exceptional functionalities of CNC aerogels that make them a potential solution to applications under challenging environments. Figure 5a illustrates the thermal insulation behavior of the unidirectional and bidirectional CNC aerogels under high and low temperature conditions. Samples with identical dimensions (20 mm length, 20 mm width, and 10 mm height) are placed on a hot/cold plate and the thermal conditions are monitored using a thermal imaging camera. As the temperature of the plate is increased to approximately 88°C, the upper surface of the unidirectional samples reaches 39.5°C while the bidirectional sample reaches approximately 37°C. Similarly, when the plate temperature is reduced to -40°C, the upper surfaces of the unidirectional and bidirectional sample reach 5.7°C and 8.4°C, respectively. Thus, while

further in-depth investigations are necessary, these results indicate that similar to other high porosity aerogels, [36] the 3D freeze printed CNC aerogels exhibit desirable thermal insulation properties, which may be tuned by controlling the pore directionality. Figures 5b and 5c compare the flammability of a unidirectional CNC aerogel sample with that of a polyurethane acoustic foam sample. As both samples are ignited simultaneously, the CNC aerogel proved considerably more resistant to ignition than the polyurethane foam. Additionally, the polyurethane foam exhibited a more vigorous combustion and burnt at a faster rate as compared to the CNC aerogel sample. Figures 5d and 5e compare the dissolvability of un-crosslinked and crosslinked unidirectional CNC aerogels. When the aerogels are submerged in water without stirring, the un-crosslinked aerogel quickly dissolves, whereas the crosslinked aerogel effectively maintains its structure. This demonstrates the crosslinked CNC aerogel's potential to withstand high humidity environments without structural failure. The above results show that 3D freeze printed CNC aerogels with controlled pore network properties are a highly attractive sustainable solution for the design of multifunctional noise reduction technologies.

3. Conclusion

We have demonstrated the 3D freeze printing of CNC aerogels with tailorable pore orientations for multifunctional noise reduction applications. The orientation of the microporous network was controlled by replacing the uniform print bed with a flat print substrate composed of PDMS and aluminum wedges. In contrast with the unidirectional temperature gradient in a conventional 3DFP setup, the difference in the thermal conductivities of these two materials creates a bidirectional temperature gradient, which consequently results in a bidirectional pore orientation. Two-microphone, normal incidence acoustic impedance tube testing reveals that the bidirectional CNC aerogels provide higher sound absorption in the low- to medium-frequency regimes as compared

to the unidirectional samples. The impedance measurements were used to model the acoustical properties of the porous CNC aerogels using the JCA formulation. The model predictions show that the 3D freeze printed CNC aerogels outperform the currently used acoustical materials in their sound absorption and transmission loss properties. Notably, the unidirectional CNC aerogels provide more than 200% higher sound transmission loss over the 600 Hz to 6100 Hz range as compared to the polyimide sample of the same thickness. Mechanical testing shows that the pore orientation also affects the effective elastic stiffness and energy absorption properties. Overall, the unidirectional pore network results in a stiffer material and provides greater energy absorption. Similar to their noise reduction capabilities, the 3D freeze printed CNC aerogels demonstrate better stiffness-to-density ratios as compared to other CNC aerogels described in existing literature. Our results show that altering the thermal gradient within the print volume allows the 3D freeze printing of CNC aerogels whose pore orientations, and thus their pore dependent functional and mechanical properties, can be controlled to achieve optimal, application-specific property combinations. This study establishes a foundation for the development of sustainable porous materials featuring controlled microporous networks and intricate macrostructural shapes suitable for multifunctional noise reduction applications.

4. Experimental Section/Methods

Aerogel Fabrication

Ink preparation: The crosslinker, 1,2,3,4-Butanetetracarboxylic acid (Sigma-Aldrich, Saint Louis, MO), was initially added at a concentration of 1 $mg \cdot mL^{-1}$ to deionized (DI) water. This was followed by 30 minutes of magnetic stirring at 350 rpm until it completely dissolved. Subsequently, commercial CNC powders (CelluForce, Montreal, Canada) were gradually added to the solution

at a concentration of 15 wt.%. The ink was then homogenized using a high shear probe homogenizer (T18 basic, Ultra Turrax, IKA Works Inc., Wilmington, NC, USA) at 6,000 rpm until it became uniform. Finally, the ink underwent additional magnetic stirring at 100 rpm for another 24 hours to ensure stability. Prior to 3D freeze printing (3DFP), the CNC ink was subjected to a vacuum mixer to reduce air bubbles for 90 seconds. After vacuum mixing, the CNC ink was transferred to a 30 mL syringe for the printing process.

Extrusion: To facilitate the 3D freeze printing (3DFP) process, a commercial CNC milling machine was adapted by replacing its milling modules with a custom-made syringe pump. This syringe pump, driven by a step motor, was seamlessly integrated with the CNC controller to enable continuous ink extrusion. The ink was methodically extruded onto a cold plate (Instec, CO, USA), layer by layer, to construct a three-dimensional structure.

During 3DFP, the cold plate's temperature was meticulously controlled, initially set at 0°C and then steadily reduced at a constant rate of 10°C per minute until reaching -70°C. This temperature regulation was achieved using a proportional integral derivative (PID) algorithm within the cold plate controller, which adjusted the heating power and cooling pump flow to maintain the desired cooling rate. A liquid nitrogen cooling system, essential for this process, was fully integrated with the cold plate. This system comprised a pump, a Dewar, and a lid equipped with a stoppered port for nitrogen refilling during operation.

In unidirectional freeze casting, the ink was deposited onto a flat cold plate. As illustrated in Figure 1c, this method resulted in ice crystals propagating solely in the vertical direction, owing to the unidirectional temperature gradient. During bidirectional freeze casting, the homogeneous aluminum plate was replaced by a PDMS wedge and an aluminum wedge, each with a 20° angle and identical dimensions (90 mm length, 50 mm width, and 18.2 mm height), assembled onto a

thick plate (see Figure 1d). In this setup, the aluminum wedge was placed at the bottom, directly affixed to the cold plate, with the PDMS wedge positioned on top. The ink was then extruded onto the PDMS wedge's top surface, enabling bidirectional freeze casting.

Post-Processing: The frozen samples were then moved to a -75°C freezer and kept for 12 hours for further freezing. Next, the samples were loaded into a freeze dry system (Labconco, Kansas City, MO) at -35°C under 200mbar vacuum to fully sublimate ice for the duration of 72 hours. Then the temperature of the freeze dryer was adjusted to 25°C and kept it under 200mbar vacuum for another 1 hour. This step was to avoid the condensation of water vapor from the air on the aerogel surface. Finally, the cross-linked CNC aerogels were obtained by a thermal treatment at 120°C for 3 hours following the freeze-drying process.

Scanning Electron Microscopy

The microstructure of the CNC aerogel was characterized by scanning electron microscopy (SEM) (Phenom Pharos Desktop SEM system). The samples were attached to SEM sample holders with conductive double-side tape and sputter-coated with a thin layer of gold prior to SEM. The accelerating voltage was set at 15 kV during SEM imaging. The captured images were then analyzed using ImageJ.

Acoustic Characterization

Normal Incidence Impedance Tube Testing: The sound absorption coefficient of the 3D printed aerogel samples was determined using a normal incidence two-microphone impedance tube. This measurement process adhered to the ASTM standard E1050-19 guidelines. The setup involved a loudspeaker, powered by an amplifier, positioned at one end of the tube to produce white noise across a frequency spectrum from DC to 10 kHz. Within the tube, which had a diameter of 30 mm, two microphones were placed 22.5 mm apart. These microphones were responsible for measuring

the plane wave pressure fields over a frequency range of 600 to 6100 Hz. The data collected from these two microphones enabled the calculation of the transfer function, denoted as H_{12}. The transfer function was defined as the ratio of the pressures measured at the second microphone to that at the reference microphone. Subsequently, the reflection coefficient (R) and the sound absorption coefficient (α) were calculated as:

$$R = \frac{e^{-jks} + H_{12}}{H_{12} - e^{-jks}} e^{-2jk(l+s)} \quad (1)$$

$$\alpha = 1 - |R|^2 \quad (2)$$

where k is the wavenumber, s and l are the microphone spacing, and the distance between the front surface of the sample and its nearest microphone respectively, and j is the imaginary number given by $\sqrt{-1}$. All the tests were conducted at a sound pressure level of 90 dB.

Inverse Characterization: The acoustical transport properties of the unidirectional and bidirectional CNC aerogels were estimated using the inverse characterization approach. [32] This method involves a curve-fitting approach to estimate the acoustical transport properties that provide the best fit with the measured sound absorption curves. The 3D freeze printed CNC aerogels were modeled as rigid porous materials using the Johnson-Champoux-Allard (JCA) formulation which requires the determination of five transport parameters for modeling the acoustical behavior. [12, 32] The five transport parameters are: porosity, static airflow resistivity, tortuosity, viscous characteristic length, and thermal characteristic length. The inverse characterization method was implemented using the commercial software package, FOAM-X. The obtained transport properties were then used to predict the sound transmission loss of the sample. The properties of the other acoustical materials were obtained using previously obtained data. [33]

Mechanical Characterization: Compression tests were conducted using a Shimadzu Universal Testing Machine, to conduct compressive tests on our samples. The tests were conducted using

cubic samples with sides of length 10 mm. The testing process involved placing each sample at the center of the machine's lower stationary plate. Above it, a top plate was positioned, which then moved downwards at a constant speed of $1mm.min^{-1}$, applying compressive force to the sample. This setup ensured that the compression was evenly distributed across the sample. To accurately capture the behavior of the samples under compression, data collection was conducted at a high frequency of 100Hz. The elastic modulus was calculated from the slopes of the obtained stress-strain curves. Similarly, the energy absorption was calculated as the area under the respective stress-strain curves until the densification strain is achieved. Density is derived by dividing the sample's weight by its volume, which was determined through precise measurements of the dimensions of the cubic sample.

Acknowledgements

Financial support from the National Science Foundation (Award No. 1943445 and 2309995) and the NASA EPSCoR Cooperative Agreement Notice Grant (Award No. 80NSSC19M0153 and 80NSSC22M0221) is gratefully acknowledged. Bhisham Sharma would like to acknowledge Ola Khaleel, Amrutha Dasyam, and Esmeralda Sanchez-Torres for assistance with acoustic testing.

Conflict of Interest

The authors declare no conflict of interest.

References

[1] A. Baigi, A. Oden, V. Almlid-Larsen, M.-L. Barrenäs, K.-M. Holgers, *Ear and Hearing* **2011**, 32, 787.

[2] K. I. Hume, M. Brink, M. Basner, *Noise and Health* **2012**, 14, 297.

[3] W. Passchier-Vermeer, W. F. Passchier, *Environmental health perspectives* **2000**, 108, 123.

[4] S. Stansfeld, M. Haines, M. Burr, B. Berry, P. Lercher, *Noise and Health* **2000**, 2, 1.

[5] a)K. Sivakumaran, J. A. Ritonja, H. Waseem, L. AlShenaibar, E. Morgan, S. A. Ahmadi, A. Denning, D. S. Michaud, R. L. Morgan, *Noise & Health* **2022**, 24, 107; b)T. Münzel, T. Gori, W. Babisch, M. Basner, *European Heart Journal* **2014**, 35, 829.

[6] a)B. Roberts, R. L. Neitzel, *The Journal of the Acoustical Society of America* **2019**, 146, 3922; b)G. W. Evans, P. Lercher, M. Meis, H. Ising, W. W. Kofler, *The Journal of the Acoustical Society of America* **2001**, 109, 1023.

[7] W. H. Organization, *Burden of disease from environmental noise: Quantification of healthy life years lost in Europe*, World Health Organization. Regional Office for Europe, **2011**.

[8] G. Shannon, M. F. McKenna, L. M. Angeloni, K. R. Crooks, K. M. Fristrup, E. Brown, K. A. Warner, M. D. Nelson, C. White, J. Briggs, *Biological Reviews* **2016**, 91, 982.

[9] a)B. L. Johnson, M. Y. Lichtveld, *Environmental policy and public health*, CRC Press, **2017**; b)D. Jarosińska, M.-È. Héroux, P. Wilkhu, J. Creswick, J. Verbeek, J. Wothge, E. Paunović, *International Journal of Environmental Research and Public Health* **2018**, 15, 813.

[10] a)L. Lu, K.-L. Yin, R. C. de Lamare, Z. Zheng, Y. Yu, X. Yang, B. Chen, *Signal Processing* **2021**, 183, 108039; b)L. Lu, K.-L. Yin, R. C. de Lamare, Z. Zheng, Y. Yu, X. Yang, B. Chen, *Signal Processing* **2021**, 181, 107929.

[11] a)M. J. Crocker, F. M. Kessler, A. J. Price, *Noise and Noise Control: Volume 1*, Crc Press, **2018**; b)I. L. Vér, L. L. Beranek, *Noise and vibration control engineering: principles and applications*, John Wiley & Sons, **2005**.

[12] J. Allard, N. Atalla, *Propagation of sound in porous media: modelling sound absorbing materials*, John Wiley & Sons, **2009**.

[13] a)Y. Tao, M. Ren, H. Zhang, T. Peijs, *Applied Materials Today* **2021**, 24, 101141; b)S. Kishore, R. Sujithra, B. Dhatreyi, *Materials Today: Proceedings* **2021**, 47, 4700.

[14] B. G. Neto, I. Pereira, S. Futatsugi, E. Brandão, P. H. Mareze, W. Fonseca, presented at *INTER-NOISE 2018 - 47th International Congress and Exposition on Noise Control Engineering: Impact of Noise Control Engineering*, **2018**.

[15] H. S. Seddeq, *Australian Journal of Basic and Applied Sciences* **2009**, 3, 4610.

[16] G. Patterson, *Carbohydrate Polymers* **2021**, 252, 117182.

[17] a)X. Wang, C. Yao, F. Wang, Z. Li, *Small* **2017**, 13, 1702240; b)J. Wang, L. Wang, D. J. Gardner, S. M. Shaler, Z. Cai, *Cellulose* **2021**, 28, 4511; c)Y.-Y. Li, B. Wang, M.-G. Ma, B. Wang, *International Journal of Polymer Science* **2018**, 2018; d)A. Kausar, S. T. Zohra, S. Ijaz, M. Iqbal, J. Iqbal, I. Bibi, S. Nouren, N. El Messaoudi, A. Nazir, *International Journal of Biological Macromolecules* **2023**, 224, 1337; e)S. Kalia, A. Dufresne, B. M. Cherian, B. S. Kaith, L. Avérous, J. Njuguna, E. Nassiopoulos, *International Journal of Polymer Science* **2011**, 2011.

[18] a)D. Trache, A. F. Tarchoun, M. Derradji, T. S. Hamidon, N. Masruchin, N. Brosse, M. H. Hussin, *Frontiers in Chemistry* **2020**, 8, 392; b)A. Dufresne, *Materials Today* **2013**, 16, 220; c)T. Abitbol, A. Rivkin, Y. Cao, Y. Nevo, E. Abraham, T. Ben-Shalom, S. Lapidot, O. Shoseyov, *Current Opinion in Biotechnology* **2016**, 39, 76.

[19] Y. Chen, L. Zhang, Y. Yang, B. Pang, W. Xu, G. Duan, S. Jiang, K. Zhang, *Advanced Materials* **2021**, 33, 2005569.

[20] a)X. Yang, K. Shi, I. Zhitomirsky, E. D. Cranston, *Advanced Materials* **2015**, 27, 6104; b)M. Hamedi, E. Karabulut, A. Marais, A. Herland, G. Nyström, L. Wågberg, *Angewandte Chemie International Edition* **2013**, 52, 12038.

[21] a)D. Bendahou, A. Bendahou, B. Seantier, Y. Grohens, H. Kaddami, *Industrial Crops and Products* **2015**, 65, 374; b)B. Seantier, D. Bendahou, A. Bendahou, Y. Grohens, H. Kaddami, *Carbohydrate Polymers* **2016**, 138, 335.

[22] a)J. Fu, S. Wang, C. He, Z. Lu, J. Huang, Z. Chen, *Carbohydrate polymers* **2016**, 147, 89; b)H. Abdul Khalil, A. Adnan, E. B. Yahya, N. Olaiya, S. Safrida, M. S. Hossain, V. Balakrishnan, D. A. Gopakumar, C. Abdullah, A. Oyekanmi, *Polymers* **2020**, 12, 1759.

[23] a)S. Deville, *Advanced Engineering Materials* **2008**, 10, 155; b)A. E. Donius, A. Liu, L. A. Berglund, U. G. Wegst, *Journal of the Mechanical Behavior of Biomedical Materials* **2014**, 37, 88; c)X. Zhang, M. Liu, H. Wang, N. Yan, Z. Cai, Y. Yu, *Carbohydrate Polymers* **2019**, 208, 232.

[24] G. Yang, H. Tetik, J. N. Weker, X. Xiao, S. Lei, D. Lin, *Review of Scientific Instruments* **2022**, 93.

[25] a)G. Zu, J. Shen, L. Zou, W. Wang, Y. Lian, Z. Zhang, A. Du, *Chemistry of Materials* **2013**, 25, 4757; b)C. Ferraro, E. Garcia-Tuñon, V. G. Rocha, S. Barg, M. D. Fariñas, T. E. G. Alvarez-Arenas, G. Sernicola, F. Giuliani, E. Saiz, *Advanced Functional Materials* **2016**, 26, 1636; c)X. Xu, Q. Zhang, M. Hao, Y. Hu, Z. Lin, L. Peng, T. Wang, X. Ren, C. Wang, Z. Zhao, *Science* **2019**, 363, 723.

[26] a)Y. Tang, S. Gong, Y. Chen, L. W. Yap, W. Cheng, *ACS Nano* **2014**, 8, 5707; b)F. Qian, P. C. Lan, M. C. Freyman, W. Chen, T. Kou, T. Y. Olson, C. Zhu, M. A. Worsley, E. B. Duoss, C. M. Spadaccini, *Nano Letters* **2017**, 17, 7171; c)F. Qian, A. Troksa, T. M. Fears, M. H. Nielsen, A. J. Nelson, T. F. Baumann, S. O. Kucheyev, T. Y.-J. Han, M. Bagge-Hansen, *Nano Letters* **2019**, 20, 131.

[27] a)Z.-Z. Pan, H. Nishihara, S. Iwamura, T. Sekiguchi, A. Sato, A. Isogai, F. Kang, T. Kyotani, Q.-H. Yang, *ACS Nano* **2016**, 10, 10689; b)F. Deuber, S. Mousavi, L. Federer, M. Hofer,

C. Adlhart, *ACS Applied Materials & Interfaces* **2018**, 10, 9069; c)K. Yin, P. Divakar, U. G. Wegst, *Acta Biomaterialia* **2019**, 84, 231.

[28] a)Z. He, J. Liu, Y. Qiao, C. M. Li, T. T. Y. Tan, *Nano Letters* **2012**, 12, 4738; b)S. Barg, F. M. Perez, N. Ni, P. do Vale Pereira, R. C. Maher, E. Garcia-Tunon, S. Eslava, S. Agnoli, C. Mattevi, E. Saiz, *Nature Communications* **2014**, 5, 4328; c)J. Kim, N. M. Han, J. Kim, J. Lee, J.-K. Kim, S. Jeon, *ACS Applied Materials & Interfaces* **2018**, 10, 37507.

[29] a)X. Song, H. Tetik, T. Jirakittsonthon, P. Parandoush, G. Yang, D. Lee, S. Ryu, S. Lei, M. L. Weiss, D. Lin, *Advanced Engineering Materials* **2019**, 21, 1800678; b)E. Brown, P. Yan, H. Tekik, A. Elangovan, J. Wang, D. Lin, J. Li, *Materials & Design* **2019**, 170, 107689; c)H. Tetik, J. Orangi, G. Yang, K. Zhao, S. B. Mujib, G. Singh, M. Beidaghi, D. Lin, *Advanced Materials* **2022**, 34, 2104980.

[30] G. Yang, F. Li, J. Xiao, H. Tetik, N. Shah, X. Xiao, J. Li, Y. Liao, S. Lei, W. Tan, *Ceramics International* **2021**, 47, 12234.

[31] a)L. Cao, Q. Fu, Y. Si, B. Ding, J. Yu, *Composites Communications* **2018**, 10, 25; b)T. Yang, L. Hu, X. Xiong, M. Petrů, M. T. Noman, R. Mishra, J. Militký, *Sustainability* **2020**, 12, 8477.

[32] Y. Atalla, R. Panneton, *Canadian Acoustics* **2005**, 33, 11.

[33] D. T. Wevita Vidanalage Dona, Wichita State University, 2020.

[34] M. F. Ashby, *Philosophical Transactions of the Royal Society A: Mathematical, Physical and Engineering Sciences* **2006**, 364, 15.

[35] a)Y. Kobayashi, T. Saito, A. Isogai, *Angewandte Chemie International Edition* **2014**, 53, 10394; b)M. D. Gawryla, O. van den Berg, C. Weder, D. A. Schiraldi, *Journal of Materials*

Chemistry **2009**, 19, 2118; c)M. Ahmadi, A. Madadlou, A. A. Saboury, *Food Chemistry* **2016**, 196, 1016.

[36] a)S. Ahankari, P. Paliwal, A. Subhedar, H. Kargarzadeh, *ACS nano* **2021**, 15, 3849; b)S. Sen, A. Singh, C. Bera, S. Roy, K. Kailasam, *Cellulose* **2022**, 29, 4805; c)M. Koebel, A. Rigacci, P. Achard, *Journal of Sol-Gel Science and Technology* **2012**, 63, 315.